Weierstraß-Institut
für Angewandte Analysis und Stochastik

im Forschungsverbund Berlin e.V.

Preprint ISSN 0946 – 8633

Traveling wave modeling, simulation and analysis of quantum-dot mode-locked semiconductor lasers

M. Radziunas[1], A. G. Vladimirov[1], E. A. Viktorov[2]

submitted: 19th April 2010

[1] Weierstrass Institute
for Applied Analysis
and Stochastics,
Mohrenstrasse 39
D - 10117 Berlin
Germany
E-Mail: radziunas@wias-berlin.de
vladimirov@wias-berlin.de

[2] Optique Nonlinéaire Théorique,
Université Libre de Bruxelles,
Campus Plaine,
Code Postal 231,
1050 Bruxelles,
Belgium
E-Mail: evviktor@ulb.ac.be

No. 1506
Berlin 2010

2000 *Mathematics Subject Classification.* 78A60, 35Q60, 35B30.

Key words and phrases. Quantum dots, semiconductor laser, saturable absorber, mode-locking, optical mode.

2010 *Physics and Astronomy Classification Scheme.* 42.55.Px, 85.35.Be, 73.63.Kv, 42.60.Fc.

Edited by
Weierstraß-Institut für Angewandte Analysis und Stochastik (WIAS)
Mohrenstraße 39
10117 Berlin
Germany

Fax: + 49 30 2044975
E-Mail: preprint@wias-berlin.de
World Wide Web: http://www.wias-berlin.de/

Abstract

We analyze the dynamics of a mode-locked quantum-dot edge-emitting semiconductor laser consisting of reversely biased saturable absorber and forward biased amplifying sections. To describe spatial non-uniformity of laser parameters, optical fields and carrier distributions we use the traveling wave model, which takes into account carrier exchange processes between wetting layer and quantum dots. A comprehensive parameter study and an optical mode analysis of operation regimes are presented.

1 Introduction

Semiconductor lasers based on self-assembled quantum dots (QD) [1] attract significant attention due to their improved lasing threshold [2], modulation bandwidth, relative intensity noise, as well as the reduced chirp [3], temperature [4] and feedback sensitivity [5] at telecom wavelengths. The advantages of a QD material can be exploited in multi-section mode-locked (ML) lasers which are able to generate stable high intensity picosecond and even sub-picosecond pulses [6].

Adequate modeling of QD lasers should take into account carrier exchange processes between their wetting layer (WL) and quantum dots. Recently proposed models based on rate equations for QD lasers operating in a CW regime [7, 8] and delay differential equations for ML-QD lasers [9] demonstrate a qualitative agreement with some experimental observations. However, these models neglect spatial distributions of carriers and electric field envelopes, which should be taken into account in a comprehensive study of dynamics in ML-QD lasers. Therefore, we propose to incorporate the carrier exchange rate equations for a QD material (see, e.g., in Refs. [10, 11]) into the traveling wave laser model [12] that takes into account spatial non-uniformity of laser parameters and resolves spatial-temporal dynamics of carrier densities and counter-propagating complex optical fields.

In this paper we simulate and analyze a model of a ML-QD laser consisting of a reverse biased saturable absorber (SA) and a forward biased amplifying gain (G) section, see Fig. 1. We perform a comprehensive parameter study of the operation regimes in this laser by identifying type of the dynamical states as well as estimating different ML state characteristics, such as pulse width, amplitude and phase jitter, signal to noise ratio, etc..

The last part of the paper is devoted to modal analysis [13] of the calculated dynamical regimes. Namely, we perform a decomposition of spatially and temporally evolving optical fields into a series of instantaneous optical modes. By doing this we can reveal the role of separate modes in the ML regime and obtain a deeper understanding of the formation of different shapes of the calculated ML pulses. In particular, we demonstrate that the ML pulses with a strongly enhanced trailing

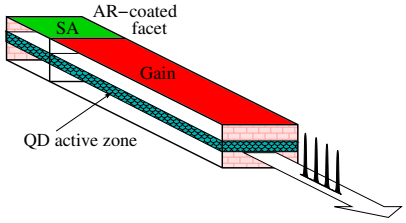

Figure 1: Sketch of a quantum-dot mode-locked laser consisting of a saturable absorber (SA) section and an amplifying section.

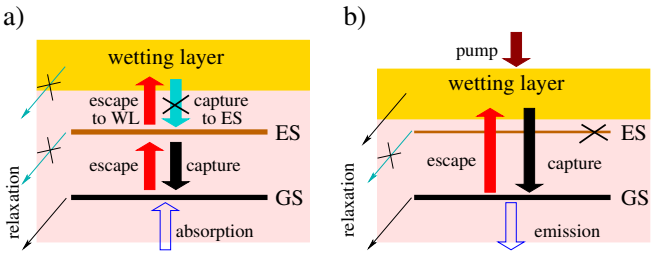

Figure 2: Schematic representation of carrier transitions in the saturable absorber section (a) and in the gain section (b).

edge can be interpreted as a superposition of a usual pulsating ML state formed by many longitudinal optical modes and a phase-shifted mode-beating type pulsation comprising only a few optical modes.

2 Mathematical model

In this paper we consider a 1+1 dimensional partial differential equation model describing spatial-temporal evolution of the counter-propagating optical fields $E^+(z,t)$, $E^-(z,t)$, material polarization functions $p^+(z,t)$, $p^-(z,t)$, carrier densities $n_{wl}(z,t)$ within the wetting layer (WL), and occupation probabilities $n_{gs}(z,t) \in [0,1]$ and $n_{es}(z,t) \in [0,1]$ of the ground state (GS) and the excited state (ES) of quantum dots, respectively.

2.1 Field equations

After fixing some reference wavelength λ_0, one can represent the main component of the electrical field in the laser as a superposition of slowly varying complex amplitudes $(E^+(z,t), E^-(z,t))$ of forward and backward propagating waves. Here, t denotes time and $z \in [0,L]$ represents a spatial position on the laser axis.

The functions $E^{\pm}(z,t)$ are governed by the traveling wave equations

$$\frac{\partial}{\partial t}\begin{pmatrix} E^+ \\ E^- \end{pmatrix}(z,t) = v_{gr}\begin{pmatrix} -\partial_z - i\beta(n,z) - \frac{\mathcal{D}}{2} & -i\kappa^-(z) \\ -i\kappa^+(z) & \partial_z - i\beta(n,z) - \frac{\mathcal{D}}{2} \end{pmatrix}\begin{pmatrix} E^+ \\ E^- \end{pmatrix} + \begin{pmatrix} F^+_{sp} \\ F^-_{sp} \end{pmatrix}, \quad (1)$$

with the reflection boundary conditions at the laser facets $z = 0$ and $z = L$

$$E^+(0,t) = r_0 E^-(0,t), \qquad E^-(L,t) = r_L E^+(L,t). \quad (2)$$

Here, $\kappa^{\pm}$ are complex coupling factors between the counter-propagating fields in the presence of Bragg grating, $v_{gr} = \frac{c_0}{n_{gr}}$ is a group velocity (c_0 – speed of light in vacuum, n_{gr} – group refractive index), $r_{0,L}$ are factors describing reflectivity of the

laser facets, and $F_{sp}^{\pm}$ represents the spontaneous emission noise [14] added to the guided waves.

Following Ref. [12] we supplement the TW equations for $E^{\pm}(z,t)$ by a pair of equations for material polarization functions $(p^{+}(z,t), p^{-}(z,t))$. These equations define the linear material gain dispersion operator $\mathcal{D}$:

$$\mathcal{D}E^{\pm} = \bar{g}\left(E^{\pm} - p^{\pm}\right), \qquad \frac{\partial}{\partial t}p^{\pm}(z,t) = \bar{\gamma}\left(E^{\pm} - p^{\pm}\right) + i\bar{\omega}p^{\pm}. \tag{3}$$

The material gain dispersion (i.e., the gain profile frequency dependence) is assumed to be Lorentzian. Parameters $\bar{g}$, $\bar{\omega}$ and $2\bar{\gamma}$ define the height of Lorentzian, the frequency of its peak position (relative to $\omega_0 = \frac{2\pi c_0}{\lambda_0}$), and its full width at half maximum, respectively. We restrict our study to a single-Lorentzian gain dispersion and assume that the laser operates at the GS transition only. The propagation factor $\beta(n,z)$ entering Eq. (1) in this case depends only on the ground state occupation probability n_{gs}:

$$\beta(n,z) = \beta(n_{gs}(z,t),z) = \delta - i\frac{\alpha}{2} + \frac{(i-\alpha_H)}{2}g'(2n_{gs}-1). \tag{4}$$

Here, δ, α, α_H and g' represent the static detuning from the reference wavelength, the internal absorption, the linewidth enhancement (Henry) factor, and the effective differential gain, respectively.

2.2 Carrier equations

Rate equations describing carrier exchange processes between wetting layer and two discrete levels in quantum dots can be found in Ref. [10]. In this paper we use a further simplified version of these equations where the carrier dynamics in each of the two laser sections is described by a pair of coupled rate equations [5, 11]. The corresponding carrier transitions are illustrated in panels (a) and (b) of Fig. 2. In the absorber section ($z \in [0, l_{SA}]$) these equations govern the time evolution of the ES and GS occupation probabilities, n_{es} and n_{gs}:

$$\begin{cases} \frac{d}{dt}n_{gs}(z,t) = -\frac{n_{gs}}{\tau_{gs}} + 2\left(\frac{n_{es}(1-n_{gs})}{\tau_{es\to gs}} - \frac{n_{gs}(1-n_{es})}{2\tau_{gs\to es}}\right) - v_{gr}g'(2n_{gs}-1)\frac{|E|^2}{2\theta_E} \\ \frac{d}{dt}n_{es}(z,t) = -\frac{n_{es}}{\tau_{es\to wl}} - \left(\frac{n_{es}(1-n_{gs})}{\tau_{es\to gs}} - \frac{n_{gs}(1-n_{es})}{2\tau_{gs\to es}}\right) \end{cases}. \tag{5}$$

In the gain section ($z \in [l_{SA}, L]$) we have a pair of rate equations for the GS occupation probability n_{gs} and the WL carrier density n_{wl}:

$$\begin{cases} \frac{d}{dt}n_{gs}(z,t) = -\frac{n_{gs}}{\tau_{gs}} + \left(\frac{n_{wl}(1-n_{gs})}{2\tau_{wl\to gs}} - \frac{n_{gs}}{\tau_{gs\to wl}}\right) - v_{gr}g'(2n_{gs}-1)\frac{|E|^2}{2\theta_E} \\ \frac{d}{dt}n_{wl}(z,t) = \frac{I}{e\theta_I} - \frac{n_{wl}}{\tau_{wl}} - 2\left(\frac{n_{wl}(1-n_{gs})}{2\tau_{wl\to gs}} - \frac{n_{gs}}{\tau_{gs\to wl}}\right) \end{cases}. \tag{6}$$

Here, $\tau_{a\to b}^{-1}$, $a, b \in \{gs, es, wl\}$ denote transition rates between GS, ES and WL, and τ_{gs}^{-1}, τ_{wl}^{-1} are spontaneous relaxation rates of the GS and WL, respectively. Apart

from the capturing rate from the exited state to the wetting layer the parameter $\tau_{es\to wl}^{-1}$ in Eq. (5) includes also a significantly smaller spontaneous relaxation rate from the ES. Factors $(1-n_{es,gs})$ in Eqs. (5,6) represent the Pauli blocking. Factor 2 in these equations accounts for the spin degeneracy in the QD energy levels, and e is the electron charge. θ_I and $\theta_E = \frac{v_{gr}c_0 h}{(L-l_{SA})\lambda_0}\theta_I$ (h is the Planck constant) are scaling factors relating injection current into the gain section I and the field intensity $|E|^2$ with the quantum dot density and the cross-section area of the active zone.

3 Numerical results

We have performed a comprehensive one- (injection current) and two- (voltage/current) parameter study of the model of two-section ML laser schematically represented in Fig. 1 and defined by Eqs. (1-6) with the parameters given in Table 1.

Table 1: Laser parameters.

central wavelength	λ_0	1.3	μm	GS relaxation time	τ_{gs}	1	ns
group refractive index	n_{gr}	3.75		WL relaxation time (G)	τ_{wl}	1	ns
total length	L	1	mm	ES to WL transition rate (SA)	$\tau_{es\to wl}$	$18\,e^{U/2}$	ps
SA length	l_{SA}	100	μm	ES to GS transition time (SA)	$\tau_{es\to gs}$	2	ps
field coupling	$\kappa^{\pm}$	0	cm^{-1}	GS to ES transition time (SA)	$\tau_{gs\to es}$	5	ps
static detuning	δ	0	cm^{-1}	WL to GS transition time (G)	$\tau_{wl\to gs}$	5	ps
internal absorption	α	5	cm^{-1}	GS to WL transition time (G)	$\tau_{gs\to wl}$	80	ps
Henry factor	α_H	0;2		voltage (SA)	U	[-8,0]	V
differential gain (SA)	g'	200	cm^{-1}	injection current	I	[0,0.8]	A
differential gain (G)	g'	40	cm^{-1}	field scaling factor	θ_E	0.0795	W
Lorentzian height	$\bar{g}$	20	cm^{-1}	injection scaling factor	θ_I	$5.85\cdot 10^6$	
Lorentzian peak freq.	$\bar{\omega}$	0	ps^{-1}	left facet reflectivity	r_0	$-\sqrt{0.95}$	
Lorentzian width	$2\bar{\gamma}$	1.8	ps^{-1}	right facet reflectivity	r_L	$\sqrt{0.3}$	

One of the most important parameters of passively ML semiconductor lasers, which can be easily tuned in experiments, is the negative voltage U applied to the SA section. Since in principle all the carrier transition rates in Eq. (5) can depend on this parameter, up to now we did not include it into the model equations (1-6) explicitly. Below, following Ref. [11], we will assume that all the transition rates but $\tau_{es\to wl}$ are independent of U, while $\tau_{es\to wl}$ shows an exponential dependence on U as given in Table 1.

3.1 Mode-locking pulsations and their characterization

Some typical nearly-perfect fundamental mode-locking pulsations are represented in Fig. 3. Panels (a,c) of this figure represent $\approx$ 25ps periodic time traces. This periodicity corresponds to the field round-trip time $T = \frac{2L}{v_{gr}}$ in the laser cavity. In the case of a fundamental ML regime, a single pulse travels along the laser cavity and

is sequentially emitted at the SA and gain section facets, see functions $|E^-(0,t)|^2$ and $|E^+(L,t)|^2$ in panel (c), respectively. A fast increase of the carrier functions n_{gs} and n_{es} shown in panel (a) corresponds to a fast saturation of the absorber section when an optical pulse passes through it and is emitted at its facet. The gain section carrier functions n_{gs} and n_{wl} have two local minima within one period of ML pulsations. Each of them corresponds to the time when an optical pulse is leaving the gain section (compare these minima with the location of optical pulses in panel (c) of Fig. 3).

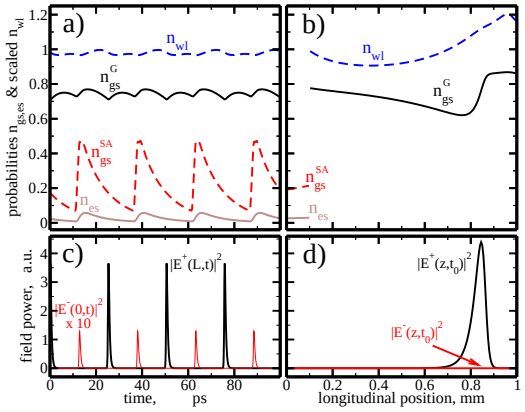

Figure 3: Typical fundamental ML pulsation ($\alpha_H = 0$, $U = -4$V, $I = 0.3$A). Left: time traces of the carrier functions $n_{gs,es,wl}$ averaged over the corresponding sections (a) and the emitted field intensities (c). Right: axial distributions of the carrier functions (b) and the optical fields (d) at some fixed time point t_0.

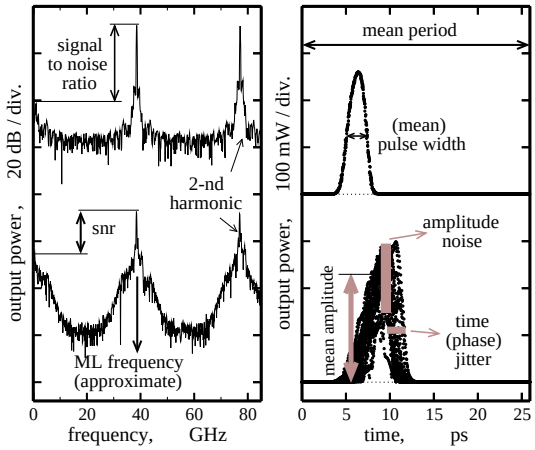

Figure 4: Characteristics of ML regime. Estimation of signal-to-noise ratio, pulsation period or frequency, mean pulse width, mean pulse amplitude, amplitude noise and time (phase) jitter from the radio-frequency spectra (left) and the sampling diagrams (right).

Panels (b) and (d) in Fig. 3 show axial distributions of carrier and field functions at some fixed time point. The power of electromagnetic field is concentrated within a single pulse traveling along the laser cavity, see function $|E^+(z,t_0)|^2$ in Fig. 3d). Panel (b) shows the depletion of carriers in the gain section by a pulse traveling in forward direction, which leads to the appearance of local minima of the gain section carrier functions in Fig. 3a).

The ML pulsations shown in Fig. 3 change their shape, period and width when changing the laser parameters. At some parameter values the transitions (bifurcations) to qualitatively different pulsating, stationary, or chaotic states can occur. Thus, an automatic identification of operation regimes and a characterization of ML pulses become very important tasks when performing theoretical or experimental parameter scans and looking for most appropriate laser operation conditions [15]. In our case the type of operation regimes and ML pulse characteristics are determined from $\sim 10-40$ns time traces of the optical field intensity $|E^+(L,t)|^2$ emitted at the gain section facet. A schematic representation of the most important automatically

recorded characteristics is given in Fig. 4. By calculating radio-frequency (RF) spectra (left part of Fig. 4) we find an approximate ML frequency[1] and a signal-to-noise ratio (snr). 30dB snr is a typical criterion for the detection of a perfect ML in our simulations or in the experiments of our technology partners [15]. By analyzing the time traces sampled with their mean period of pulsations [14] (right part of Fig. 4) we get an additional information about the pulse width, the time (phase) jitter, or the amplitude noise of ML pulsations. The automatic sampling of pulses and definition of some pulse characteristics mentioned above are working perfectly for regular ML pulses, but become more complicated and even can fail for Q-switched ML or irregular quasi- or non-periodic pulsations containing two or more different pulses within the time interval T.

3.2 One- and two- parameter analysis

In this section we present a typical one- and two-parameter study of the considered ML laser model.

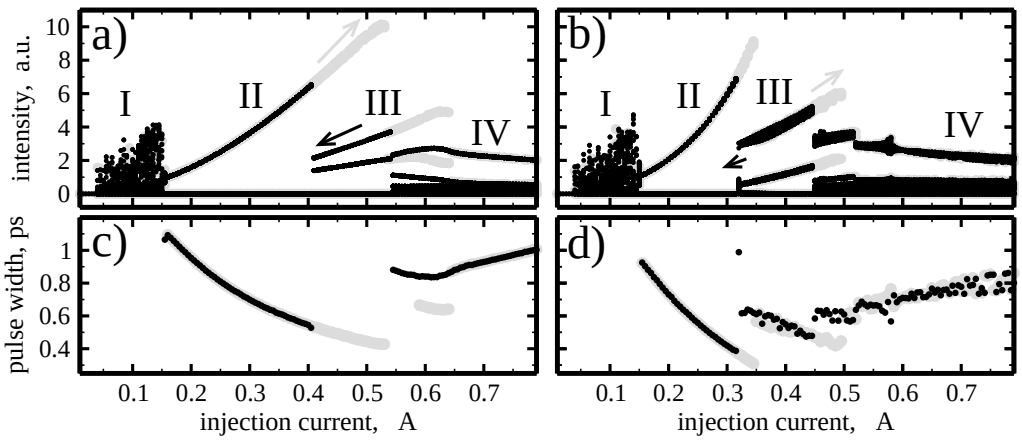

Figure 5: One-parameter continuation diagrams for increased (grey) and decreased (black) injection currents at fixed $U = -6$V and $\alpha_H = 0$ (a,c) or $\alpha_H = 2$ (b,d). (a) and (b): local minima and maxima of simulated time trace $|E^+(L,t)|^2$. (c) and (d): mean width of ML pulses.

Fig. 5 represents two typical sequences of different pulsing states obtained in our simulations. Let us discuss the case when $\alpha_H = 0$ which corresponds to the panels (a,c) of this figure. At lower injections currents ($I \leq 0.03$A) the laser is off, as it is indicated by zero intensity in Fig. 5a). Above the lasing threshold for $I < 0.16$A the laser operates in a Q-switched ML regime [15] (region I) characterized by the T-separated pulse packages reappearing with 1-4 GHz Q-switching frequency.

[1]For a fundamental ML regime this frequency is close to $\frac{1}{T}$. In some cases, however, harmonic ML [15] can be observed with the main frequency peak at $\sim \frac{j}{T}$, $j = 2, 3, \ldots$ and a strong suppression of lower harmonic peaks at $\sim \frac{k}{T}$, $k = 1, \ldots, j-1$.

At higher injections a fundamental ML regime (region II) appears similar to that represented in Fig. 3. Fig. 5c) illustrates the decrease of ML pulse width with the increase of injection current I for this regime. With further increase of the injection current our simulations show transitions to other $\sim T$-periodic regimes such as a solution with two non-equal pulses in the cavity indicated by III and Fig. 6b(D) and a solution with a single short pulse having a long oscillating trailing edge, see regime IV and Fig. 6b(C). Noteworthy, that the increase of an injection in the latter regime leads to a broadening of ML pulses, see panel c) of Fig. 5. With decrease of the injection current we observe again regimes I to IV. For different directions of injection tuning, however, the transitions between corresponding regimes occure at different positions.

All these regimes are preserved after an inclusion of a nonzero α_H factor, see panels (b,d) of this figure. However, the stability range of the fundamental ML regime II becomes smaller, while the amplitude noise and time jitter of the regimes III and IV increase, see, e.g., increased dispersion of maximal amplitudes at $I > 0.35A$ in Fig.5b).

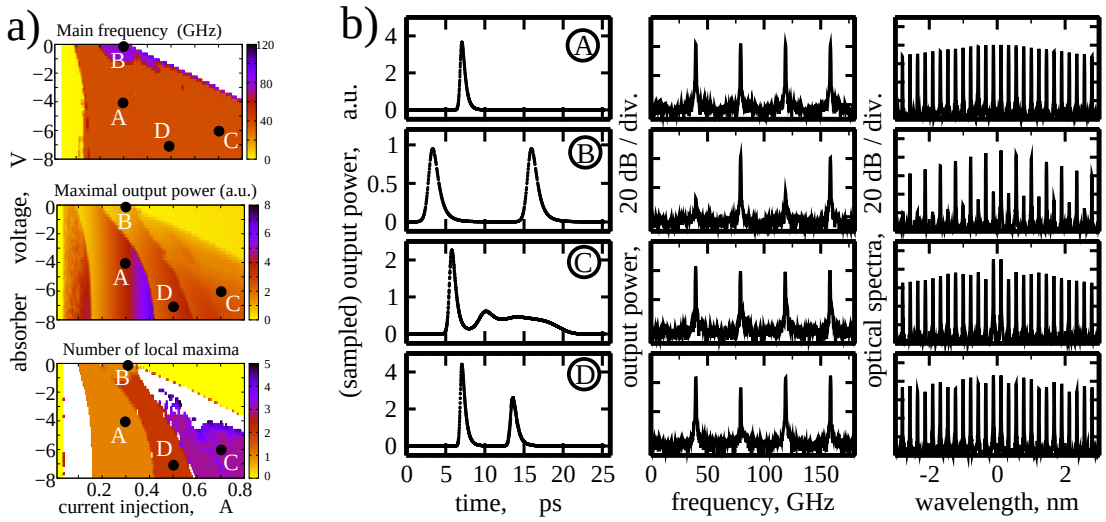

Figure 6: Two-parameter analysis of ML laser model with $\alpha_H = 0$. (a): representation of the simulated mean frequency (top), the maximal output power (middle) and the number of distinguishable local maxima per sampling period (bottom) in the injection/voltage plane. (b): sampling diagram (left), RF spectra (middle), and optical spectra (right) of four typical periodic solutions corresponding to injection & voltage values shown by bullets (A-D) in panel (a). (A): pure ML. (B): 2-nd harmonic ML. (C): stable $\sim T$-periodic ML with a long trailing edge. (D): double-pulse $\sim T$-periodic solution.

We have performed a series of one-parameter scans discussed above for different values of voltage U. Some results of these simulations[2] are summarized in Figure 6.

[2]During the simulations the following steps have been performed: i) set $U = 0$V and $I = 0.8$A;

The mean frequency f diagram shown in the upper panel of Fig. 6a) indicates the parameter regions of QS ML pulsations ($f < 10$GHz), different T-periodic regular or irregular pulsations ($f \approx 40$GHz), harmonic ML ($f \approx 80$GHz), and continuous wave states (white regions). The maximal power diagram presented in the middle panel of this figure allows to recognize the transitions between different pulsating regimes. The diagram showing the number of local intensity maxima per mean period of pulsations, see bottom panel of Fig. 6a), distinguishes between irregular (e.g. QS ML) and different types of regular pulsations. Fig. 6b) presents several periodic solutions from different two-parameter regions discussed above.

Let us now briefly discuss an important imperfection of our analysis. In general, the fundamental ML pulse-width, in our simulations, decreases with the injection current (see region II in Fig. 5), what contradicts to the most of experimental results. We have analyzed the possible factors leading to the pulse-width broadening and found two most relevant nonlinear impacts: the role of ES in amplifying section, and nonlinear gain compression due to the spectral/spatial hole burning. It is difficult to distinguish the possible relative contribution of these two effects to the pulse broadening. On the one hand, the presence of ES is slowing down the GS carrier relaxations (aka phonon bottleneck) what, in turn, implies a broadening of ML pulses. On the other hand, the nonlinear gain compression which can be used to account for the multiple types of spectral hole burning effects in quantum dot lasers [16] is known to play a significant role in the pulse-width increase in passively ML QD lasers [15]. More detailed analysis and simulations of these two factors leading to the pulse broadening will be discussed elsewhere.

4 Modal analysis

To obtain a deeper understanding of the formation mechanisms of stable ML pulses with a long trailing edge, see Fig. 6b(C), we perform a modal analysis [13] of the computed optical fields. First, we rewrite the field equations (1-3) in the operator form:

$$\frac{d}{dt}\Psi(z,t) = H(\beta)\Psi(z,t), \quad \text{where} \quad \Psi \stackrel{def}{=} \left(E^+, E^-, p^+, p^-\right)^T. \tag{7}$$

Then, for each fixed $\beta(z)$, we consider the spectral problem for the operator $H(\beta)$:

$$\begin{array}{ll} [H(\beta) - i\Omega]\,\Theta(z) = 0, & \Theta \stackrel{def}{=} \left(\Theta_E^+, \Theta_E^-, \Theta_p^+, \Theta_p^-\right)^T, \\ \Theta_E(z) \quad \text{satisfies b.c. (2)}, & \text{scaling:} \quad \Theta_E^+(\beta, L) = 1. \end{array} \tag{8}$$

Here, the complex frequency Ω and the eigenfunction Θ determine an *instantaneous* (carrier- or β- dependent) optical mode. $\Re e\Omega$ and $\Im m\Omega$ are the angular frequency and the damping rate of the optical mode, respectively.

ii) simulate transients and save final field/carrier distributions; iii) tune I down to 0A recording main characteristics of trajectories; iv) set again $I = 0.8$A, decrease slightly U, set in the step ii) saved distributions as initial conditions and proceed with the step ii).

At each time point t we freeze the value of the propagation factor $\beta(z,t)$ and decompose the field function $\Psi(z,t)$ computed numerically into series of instantaneous modes:

$$\Psi(z,t) = \sum_k f_k(t)\Theta_k(\beta,z) \qquad \Longrightarrow \qquad E^+(L,t) = \sum_k f_k(t), \tag{9}$$

where f_k are complex mode amplitudes which represent the contribution of k-th mode to the field emitted from the gain section facet.

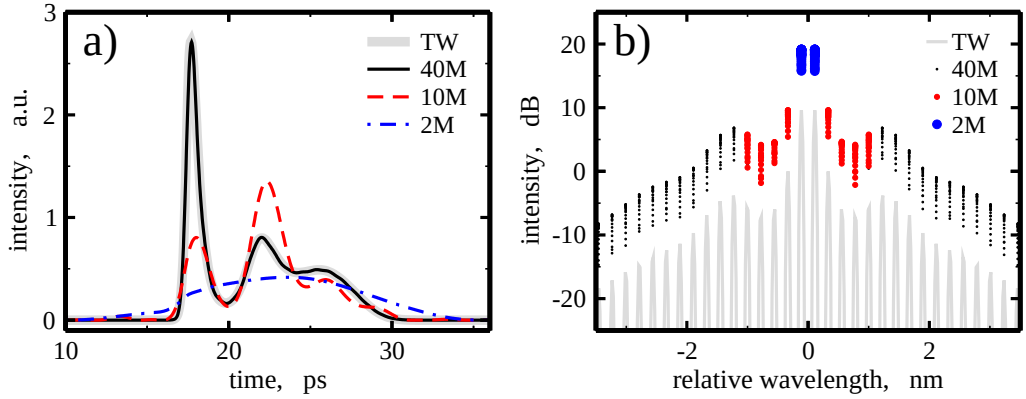

Figure 7: Modal analysis of a stable ML pulse with a long trailing edge ($\alpha_H = 0$, $U = -5.5$V, $I = 0.6$A). (a): calculated temporal trace of the field intensity emitted at the gain section facet (thick) and its reconstruction from 40, 10 and 2 modes with largest amplitudes $|f_k|$ (thin). (b): optical spectra of the emitted field (line) and parametric representation of amplitudes $|f_k(t)|$ vs. modal wavelengths $\sim \Re e\Omega_k(t)$ (bullets). Bullets of different sizes indicate modes used for the field reconstruction in panel (a).

The shape of a ML pulse depends strongly on the relations between the intensities and phases of the complex modal amplitudes. Since the mode decomposition (9) of the optical field provides an access to these amplitudes, one can easily inspect the role of different modes on the formation of ML pulsations.

An example illustrating our modal analysis is presented in Fig. 7. In this example, total number of 200 modes centered around the gain peak frequency have been used in the decomposition of the field function $\Psi(z,t)$. Fig. 7a) presents an attempt to reconstruct the electric field amplitude from the modal expansion by taking into account only $n \ll 200$ modes having largest amplitudes ($n = 2, 10, 40$). It is seen from this figure that 40-mode field reconstruction approximates almost perfectly the full field function. On the other hand, 2- or 10-mode reconstructions are not sufficient to recover the calculated pulse shape.

The comparison of n-mode reconstructions of $\Psi(z,t)$ with different n shows also another interesting feature of the solution presented in Fig. 6b(C). In usual ML state an addition of new phase-locked modes to already locked set of modes results in an increase of pulse amplitude and a decrease of pulse width without a significant

shift of the pulse peak position. In our case, however, when increasing the number n from 2 to 40 the peak position of the reconstructed pulse shifts by $\sim 25\%$ of the pulsation period. This indicates that the strong asymmetry in pulse shape is not only due to a larger contribution of the pair of central modes (as it is seen from the optical spectra shown in Fig. 7b)) but also due to specific phase relations between these two and the remaining modes. In other words, the optical field corresponding to the asymmetric pulse shown in Fig. 6b(C) can be represented as a superposition of two optical fields. The first of them comprises only two central modes[3] with largest amplitudes and demonstrates sinus-like pulsations in time. The second field comprising only part of the above mentioned two modes and all remaining modes demonstrates nearly-perfect ML pulsations. The periodicities of these two pulsating fields are identical, but the pulse peak positions are shifted from one another.

5 Conclusions

We have developed a model of an edge-emitting QD laser based on the TW equations for optical field amplitudes of two counter-propagating waves coupled to the rate equations for carrier exchange processes in the quantum-dots and the wetting layer. We use this model for a numerical simulation of dynamical regimes in a mode-locked laser consisting of a reversely biased saturable absorber and a forward biased gain section. We perform one- and two- parameter study of this laser using several techniques which allow an automatic classification of operation regimes as well as a calculation of different characteristics of pulsating regimes. Finally, we demonstrate how a mode decomposition of an optical field helps to interpret an asymmetry of ML pulses.

Acknowledgments

The work of M. Radziunas was supported by DFG Research Center MATHEON "Mathematics for key technologies: Modelling, simulation, and optimization of real-world processes". A. G. Vladimirov acknowledges the support from SFB 787 project of the DFG.

References

[1] D. Bimberg, M. Grundmann, and N.N. Ledentsov, *Quantum dot heterostructures*, J. Willey, 1999.

[3] In the case of non-vanishing α_H the number of modes forming the first field is still low but not so clearly defined.

[2] G. Park, O.B. Shchekin, D.L. Huffaker, and D.G. Deppe, "Low-threshold oxide-confined 1.3-μm quantum-dot laser," *IEEE Photon. Technol. Lett.* **12**, pp. 230–232, 2000.

[3] H. Saito, K. Nishi, A. Kamei, and S. Sugou, "Low chirp observed in directly modulated quantum dot lasers," *IEEE Photon. Technol. Lett.* **12**, pp. 1298–1300, 2000.

[4] R. Debusmann, T.W. Schlereth, S. Gerhard, W. Kaiser, S. Höfling, and A. Forchel, "Gain studies on quantum-dot lasers with temperature-stable emission wavelength," *IEEE J. Quantum Electron.* **44**, pp. 175-181, 2008.

[5] D. O'Brien, S.P. Hegarty, G. Huyet, and A.V. Uskov, "Sensitivity of quantum-dot semiconductor lasers to optical feedback," *Opt. Lett.* **29**, pp. 1072–1074, 2004.

[6] E.U. Rafailov, M.A. Cataluna, and W. Sibbett, "Mode locked quantum-dot lasers," *Nat. Photon.* **1**, pp. 395–401, 2007.

[7] A. Markus, J.X. Chen, O. Gauthier-Lafaye, J.-G. Provost, C. Paranthoën, and A. Fiore, "Impact of intraband relaxation on the performance of a quantum-dot laser," *IEEE J. Selected Topics of Quantum Electron.* **9**, pp. 1308–1314, 2003.

[8] K. Lüdge, E. Schöll, "Quantum-dot lasers – desynchronized nonlinear dynamics of electrons and holes," *IEEE J. Quantum Electron.* **45**, pp. 1396–1403, 2009.

[9] E.A. Viktorov, P. Mandel, A.G. Vladimirov, and U. Bandelow, "A model for mode-locking in quantum dot lasers," *Appl. Phys. Lett.* **88**, pp. 201102, 2006.

[10] A. Markus, M. Rossetti, V. Calligari, D. Chek-Al-Kar, J.X. Chen, and A. Fiore, "Two-state switching and dynamics in quantum dot two-section lasers," *J. of Applied Physics* **100**, pp. 113104, 2006.

[11] E.A. Viktorov, T. Erneux, P. Mandel, T. Piwonski, G. Madden, J. Pulka, G. Huyet, and J. Houlihan, "Recovery time scales in a reversed-biased quantum dot absorber," *Appl. Phys. Lett.* **94**, pp. 263502, 2009.

[12] U. Bandelow, M. Radziunas, J. Sieber, and M. Wolfrum, "Impact of gain dispersion on the spatio-temporal dynamics of multisection lasers," *IEEE J. Quantum Electron.* **37**, pp. 183–188, 2001.

[13] M. Radziunas, H.-J. Wünsche, "Multisection lasers: longitudinal modes and their dynamics," in *Optoelectronic Devices - Advanced Simulation and Analysis*, J. Piprek, ed., pp. 121–150, Springer, New-York, 2005.

[14] H.-J. Wünsche, M. Radziunas, S. Bauer, O. Brox, and B. Sartorius, "Simulation of phase-controlled mode-beating lasers," *IEEE J. Selected Topics of Quantum Electron.* **9**, pp. 857–864, 2003.

[15] U. Bandelow, M. Radziunas, A. Vladimirov, B. Hüttl, and R. Kaiser, "Harmonic mode-locking in monolithic semiconductor lasers: theory, simulations and experiment," *Optical and Quantum Electronics* **38**, pp. 495–512, 2006.

[16] A.V. Uskov, Y. Boucher, J. Le Bihan, and J. McInerney, "Theory of a self-assembled quantum-dot semiconductor laser with Auger carrier capture: Quantum efficiency and nonlinear gain," *Appl. Phys. Lett.* **73**, pp. 1499-1501, 1998.